Theoretical prediction of electronic, transport, optical, and thermoelectric properties of Janus monolayers In_2XO (X = S, Se, Te)

Tuan V. Vu,[1,2,*] Chuong V. Nguyen,[3] Huynh V. Phuc,[4] A. A. Lavrentyev,[5] O. Y. Khyzhun,[6] Nguyen V. Hieu,[7] M. M. Obeid,[8] D. P. Rai,[9] Hien D. Tong,[10] and Nguyen N. Hieu[11,12,†]

[1]Division of Computational Physics, Institute for Computational Science, Ton Duc Thang University, Ho Chi Minh City 700000, Vietnam
[2]Faculty of Electrical & Electronics Engineering, Ton Duc Thang University, Ho Chi Minh City 700000, Vietnam
[3]Department of Materials Science and Engineering, Le Quy Don Technical University, Hanoi 100000, Vietnam
[4]Division of Theoretical Physics, Dong Thap University, Cao Lanh 870000, Vietnam
[5]Department of Electrical Engineering and Electronics, Don State Technical University, 1 Gagarin Square, 344010 Rostov-on-Don, Russian Federation
[6]Frantsevych Institute for Problems of Materials Science, National Academy of Sciences of Ukraine, 3 Krzhyzhanivsky Street, 03142 Kyiv, Ukraine
[7]Department of Physics, The University of Danang—University of Science and Education, Da Nang 550000, Vietnam
[8]Department of Non-metallic Materials, College of Materials Engineering, University of Babylon, Hilla 51001, Iraq
[9]Physical Sciences Research Center, Department of Physics, Pachhunga University College, Aizawl 796001, India
[10]Faculty of Engineering, Vietnamese-German University, Binh Duong 590000, Vietnam
[11]Institute of Research and Development, Duy Tan University, Da Nang 550000, Vietnam
[12]Faculty of Natural Sciences, Duy Tan University, Da Nang 550000, Vietnam

(Received 23 July 2020; revised 27 January 2021; accepted 3 February 2021; published 15 February 2021)

The breaking of the vertical symmetry in Janus monochalcogenides gave rise to many properties that were not present in the original monochalcogenide monolayers. However, recent papers have often focused only on Janus monochalcogenides containing S, Se, and Te elements despite that O is also one of the group VI chalcogen elements. In this paper, we systematically investigate the electronic, transport, optical, and thermoelectric properties of Janus monolayers In_2XO (X = S, Se, Te) using first-principles calculations. Based on phonon spectrum analysis and *ab initio* molecular dynamics simulations at room temperature, In_2XO monolayers were reported to be stable. Our calculations reveal that, while In_2SO is an indirect semiconductor, In_2SeO exhibits a direct semiconducting characteristic, and biaxial strain can lead to the semiconductor-metal phase transition in In_2SeO. Monolayer In_2TeO is metal at equilibrium, and its metallic characteristics are prevented under biaxial strains. Calculations for transport properties show that the carrier mobilities of In_2SO and In_2SeO monolayers are highly anisotropic, and electron mobility of In_2SO exceeds 3×10^3 cm^2/Vs. In this paper, the optical and thermoelectric properties of In_2SO and In_2SeO monolayers are also investigated and discussed in detail. Finally, the electronic properties of all four possible stacking configurations of the Janus bilayers are briefly calculated. Our findings not only contribute to a more general view of the physical properties of the Janus group III monochalcogenides but also recommend them as potential nanomaterials for applications in optoelectronic and thermal devices.

DOI: 10.1103/PhysRevB.103.085422

I. INTRODUCTION

For more than a decade, two-dimensional (2D) layered nanomaterials have been hot topics that have attracted many scientists because of their outstanding electronic, mechanical, and chemical properties [1–3]. The 2D family, starting with graphene [4], is increasingly expanding. Many 2D nanomaterials have been recently discovered one after the other, from silicene [5] to transition metal dichalcogenides (TMDs) [6,7] and other graphenelike structures [8,9]. The 2D monolayers possess many extraordinary physical properties which do not exist in bulk materials [10–13]. Recently, a series of group III monochalcogenide nanosheets, including GaS [14,15], GaSe [14,16], InS [17], and InSe [18], has been experimentally synthesized. Also, theoretical studies have indicated that the group III monochalcogenide monolayers [19] have potential applications in optoelectronic devices [20] and photocatalytic water splitting technology [21,22].

Recently, Janus monolayers of TMDs joined the 2D family as additional members. Two research groups [23,24] independently reported that Janus MoSSe with an asymmetric structure was successfully synthesized experimentally. Indeed, the success of the synthesis of MoSSe has initiated a series of studies on Janus structures [25–28]. The future of Janus structures is considered bright with many prospects for application in nanotechnology [29]. Using first-principles calculations, Huang *et al.* demonstrated that the Janus M_2XY

*vuvantuan@tdtu.edu.vn
†Corresponding author: hieunn@duytan.edu.vn

  ©2021 American Physical Society

(M = Ga, In; X/Y = S, Se, Te; $X \neq Y$) monolayers were semiconductors and can possess photocatalytic activity for water splitting [30]. The mirror symmetry breaking in Janus structures not only affects the electronic properties but also significantly changes their transport properties. Wan *et al.* revealed that the carrier mobility of Janus In_2SeTe is higher than that of the InSe monolayer [31]. Moreover, Janus structures of group III chalcogenides exhibit superiority in piezoelectric properties compared with pure group III monochalcogenides. The piezoelectric coefficient of the In_2SSe monolayer is up to 8.47 pm/V, more than four times higher than that obtained in pure group III monochalcogenides [32]. The piezoelectric coefficient of group III monochalcogenides MX (M = Ga, In; X = S, Se, Te) varies from 1.91 pm/V (InS) to 1.98 pm/V (InSe) [32]. Kandemir and Sahin have systematically investigated the electronic properties of the Janus In_2SSe monolayer using first-principles calculations [33]. The In_2SSe monolayer is predicted to have a hexagonal structure like InSe and InS monolayers. However, in the Janus structure, there are differences in work functions between chalcogenide sides, which lead to a major change in its electronic structures [33]. Recently, a type of Janus group III monochalcogenides, GaInSS, GaInSSe, and GaInSeSe, has been theoretically proposed [34].

A lot of papers for Janus group III monochalcogenides have been done; however, recent reports focus only on Janus structures that contain the S, Se, and Te elements. Recently, Cui *et al.* have investigated the piezoelectric properties of Janus Ga_2YZ (Y/Z = O, S, Se) monolayers using first-principles calculations [35]. They focused on the piezoelectric properties of the Ga_2YZ monolayers, and only a brief description of the band structures of the Ga_2YZ has been provided. However, in the compounds containing an O element, the band diagrams are not ordered according to the period of metal elements. This has also been verified for group III monochalcogenides ΠO (Π = B, Ga, In, Al) [19]. Very recently, the dynamical stability of the Janus MoSO monolayer [36] and electronic properties of the oxygenation of gallium monochalcogenide monolayers [37] have been investigated by first-principles calculations. Janus group III monochalcogenides containing an O element (also group VI chalcogen elements), such as monolayers In_2XO (X = S, Se, Te), have not been investigated yet. In this paper, we consider the electronic, transport, optical, and thermoelectric properties of Janus monolayers In_2XO (X = S, Se, Te) using first-principles calculations. The structural properties of all three Janus monolayers In_2XO were calculated first and their stabilities, including dynamical and thermal, were then tested via the analysis of the phonon dispersion and molecular dynamic simulations. Next, the electronic, transport, optical, and thermoelectric properties are systematically investigated in this paper. Finally, a brief investigation of the electronic properties of the bilayers of In_2SO and In_2SeO with four possible stacking configurations is presented in the last part of this paper.

II. COMPUTATIONAL DETAILS

In this paper, first-principles calculations based on density functional theory (DFT) were performed with the Quantum Espresso package [38]. We used the generalized gradient approximations of Perdew-Burke-Ernzerhof (PBE) [39] to investigate the exchange-correlation interaction. The DFT-D2 method proposed by Grimme [40] was used to consider the effect of the long-range weak van der Waals interactions in Janus structures. Also, spin-orbit coupling (SOC) was included in self-consistent calculations for electronic structures for the Janus In_2XO monolayers [41]. The cutoff energy for the plane-wave basis was set to be 500 eV. We used a $(15 \times 15 \times 1)$ k-mesh to sample the Brillouin zone (BZ). The structure is optimized when the forces on atoms are less than 10^{-3} eV/Å. To eliminate interactions between neighbor slabs, a vacuum space of 20 Å was inserted into the vertical direction of the 2D surface. Additionally, we used the Heyd-Scuseria-Ernzerhof hybrid functional (HSE06) to correct the band structures of the Janus structures.

The dynamical stability was checked via calculations for the phonon spectrum by using the density functional perturbation theory method [42] via the Quantum Espresso simulation package [38]. A large supercell of $8 \times 8 \times 1$ was constructed for the phonon calculations to guarantee the convergence and give accurate results. Also, we performed the *ab initio* molecular dynamics (AIMD) simulations [43] at room temperature for 5 ps with 5000 time steps to test the thermal stability of the Janus In_2XO structures. The canonical ensemble (NVT) with constant temperature was used for the calculations of thermal characteristics. The thermoelectric properties were investigated through the semiclassical Boltzmann transport theory as performed in the BoltzTrap code [44]. The lattice thermal conductivity was calculated by using the Phono3py package [45]. We used a $90 \times 90 \times 1$ k-point mesh to sample the BZ in calculations for the transport coefficients.

III. STRUCTURE AND STABILITY

The Janus In_2XO monolayers (X = S, Se, Te) can be built from the group III monochalcogenide monolayer InO by replacing one layer of O atoms by another layer of X atoms. While the group III monochalcogenides belong to the D_{3h} symmetry group with mirror symmetry, the breaking of a minor symmetry in the Janus In_2XO monolayers make them belong to the $P3m1$ (C_{3v}) space group. The geometric structure plays a decisive role in determining the electronic and transport properties of 2D nanomaterials. The absence of mirror symmetry in the Janus In_2XO monolayers is expected to introduce physical properties which do not exist in the monochalcogenide monolayers. The optimized atomic structure of the Janus In_2XO monolayer is illustrated in Fig. 1(a). After full relaxation, the calculated lattice constant of the Janus In_2SO monolayer was $a = 3.699$ Å. Our obtained results demonstrate that the lattice constant of the Janus In_2XO monolayer increases with the increase in the size of the element X, from S to Te. Similarly, the In-In, In-X, and In-O bond lengths d in the Janus In_2XO structures increase when the element X moves down in the chalcogen group, from S to Te. Also, when the chalcogen atom moves down from S to Te, while the X-In-In bond angle increases, the In-In-O bond angle is decreased. The calculated structural parameters of the Janus In_2XO monolayers are summarized in Table I. Compared with the available data for the In-based

TABLE I. The calculated lattice constant a, bond length d, thickness, bond angle θ, and cohesive energy E_{coh} of the Janus In_2XO (X = S, Se,Te) monolayers.

	a (Å)	$d_{In\text{-}In}$ (Å)	$d_{In\text{-}X}$ (Å)	$d_{In\text{-}O}$ (Å)	Thickness (Å)	$\phi_{\angle XInIn}$ (deg)	$\phi_{\angle InInO}$ (deg)	E_{coh} (eV/atom)
In_2SO	3.699	2.850	2.508	2.223	4.783	121.633	106.122	4.238
In_2SeO	3.761	2.851	2.601	2.245	4.853	123.379	104.735	4.082
In_2TeO	3.859	2.872	2.814	2.281	5.081	127.650	102.417	3.761

monochalcogenide monolayers (InX and InO) [19], our calculations reveal that the lattice constant and thickness of the Janus In_2XO monolayer are smaller than that of the InX monolayer but larger than that of the InO monolayer. Similarly, the In-O bond length $d_{In\text{-}O}$ in the Janus In_2XO structures (from 2.223 to 2.281 Å) is longer than that in InO (2.16 Å) [19]. Meanwhile, the $d_{In\text{-}X}$ in the Janus In_2XO structures is shorter than that in the monochalcogenides InX.

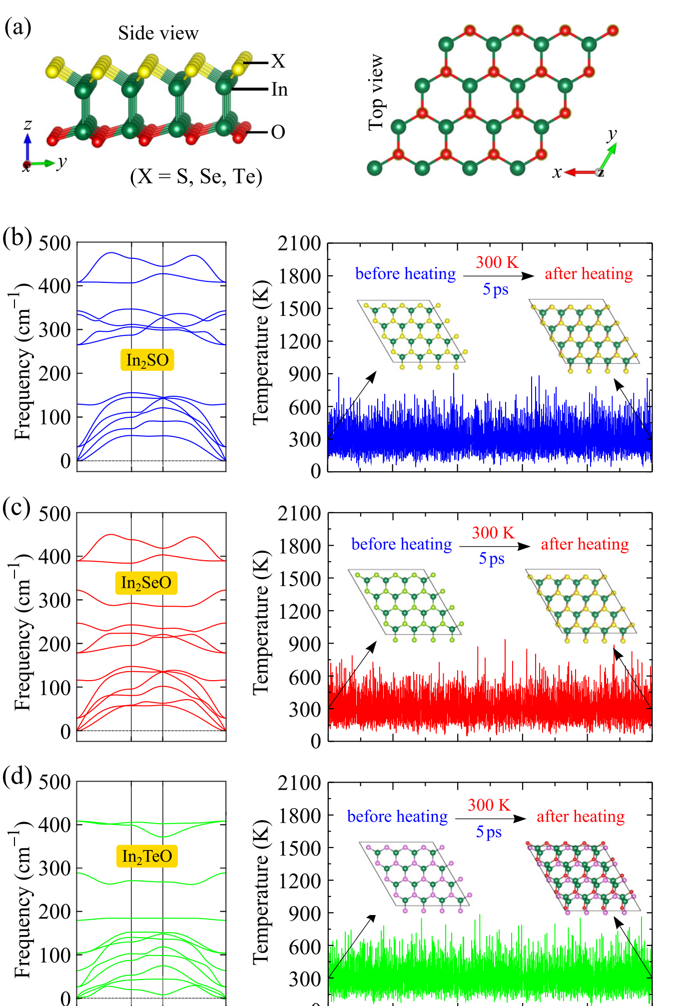

FIG. 1. (a) The side and top views of Janus In_2XO (X = S, Se, Te). Phonon spectra and *ab initio* molecular dynamics (AIMD) simulations of time-dependent temperature fluctuation at room temperature of (b) In_2SO, (c) In_2SeO, and (d) In_2TeO monolayers.

Cohesive energy E_{coh} of the Janus In_2XO monolayer is estimated using the formula

$$E_{coh} = \frac{N_{In}E_{In} + N_X E_X + N_O E_O - E_{In_2XO}}{N_{In} + N_X + N_O}, \tag{1}$$

where E_{In}, E_O, and E_X are, respectively, the single atom energies of the elements In, O, and X; E_{In_2XO} refers to the total energy of the Janus In_2XO monolayer; and N_{In}, N_O, and N_X stand for the number of the In, O, and X atoms in the unit cell, respectively. Our obtained results demonstrate that the most energetically stable structure is the Janus In_2SO monolayer with the cohesive energy of $E_{coh}^{In_2SO} = 4.238$ eV, and the Janus In_2TeO monolayer is least stable with $E_{coh}^{In_2TeO} = 3.761$ eV. These values of the cohesive energy of In_2XO monolayers are higher than recently reported for InS, InSe, and In_2SSe monolayers [33].

Further, we checked the dynamical and thermal stabilities of the Janus In_2XO monolayers via calculations for phonon dispersions and AIMD simulations. The obtained results for the phonon spectrum and AIMD simulations at room temperature of the Janus In_2XO monolayers are depicted in Figs. 1(b)–1(d). The phonon spectra of the In_2XO monolayers have 12 vibrational modes, including three acoustic modes and nine optical modes, because their primitive cell contains four atoms (two In atoms, one chalcogen X atom, and one O atoms). Focusing on the optical spectrum, which is determined via nine distinct eigenmodes, in the phonon spectra of all three Janus structures, we can see that, at the Γ point, there are three nondegenerate modes and three doubly degenerate. The frequency of the optical branches decreases from In_2SO to In_2TeO. This is related to the atomic mass of the chalcogen atoms, which increases from S to Te. Our obtained results reveal that there is no gap between the acoustic and optical branches. In all three Janus structures, there is a frequency range where both acoustic and optical modes coexist. This can cause the Janus structures to have low thermal conductivity due to the possibility of strong optical-acoustic scattering. As presented in Figs. 1(b) and (c), there are no negative frequencies in the phonon spectra of all three Janus In_2XO structures, implying that the In_2XO monolayers are dynamically stable at equilibrium.

By using AIMD simulations, we tested the thermal stability of the Janus In_2XO monolayers at room temperature (300 K). The Janus In_2XO monolayers were heat-treated at 300 K within 5 ps with 5000 time steps. The temperature fluctuation as a function of time by AIMD simulations are also shown in Figs. 1(b)–1(d). Our calculations demonstrate that the atomic structures of the Janus monolayers are still robust after 5 ps of heating. No remarkable distortions are observed in atomic structures of all three Janus monolayers, as presented in the

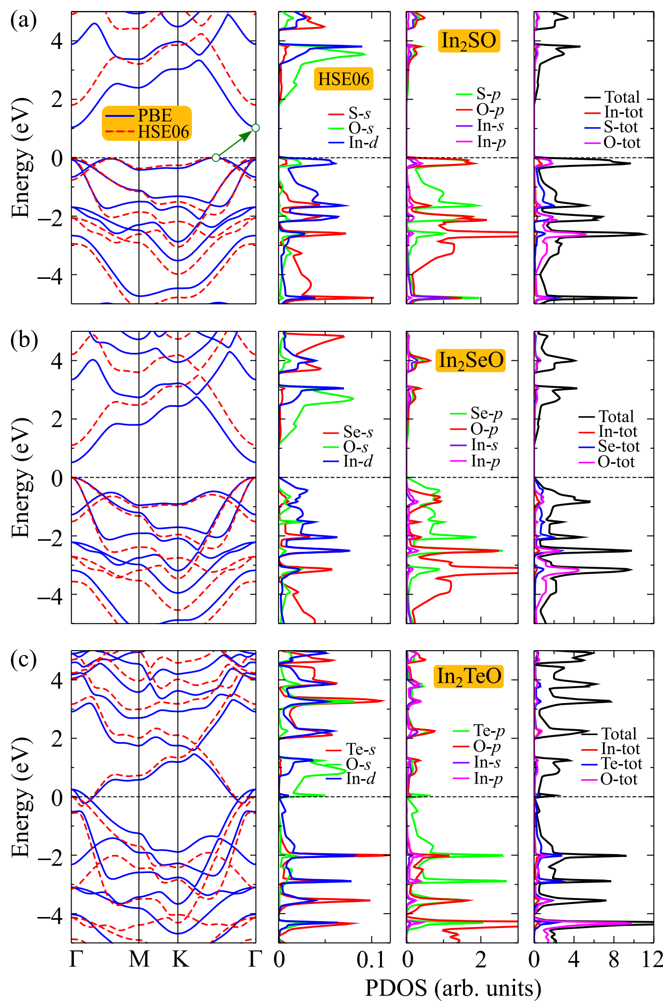

FIG. 2. Band structures and density of states of (a) In_2SO, (b) In_2SeO, (c) and In_2TeO.

snapshots of their atomic structures in Figs. 1(b)–1(d). Also, there is no structural transition as well as no bond breaking in the Janus structures at 300 K. We can conclude that the Janus In_2XO monolayers are thermally stable at room temperature.

IV. ELECTRONIC PROPERTIES

In Fig. 2, we show our calculations for the band structures along the Γ-K-M-Γ high-symmetry direction of the Janus In_2XO monolayers. At the PBE level, both In_2SO and In_2SeO monolayers exhibit semiconducting characteristics with band gaps at PBE level E_g^{PBE} being 1.084 and 0.580 eV, respectively. This is consistent with the trend that the band gap will decrease as the chalcogen atoms move down from S to Te, as happened in the group III monochalcogenides [19]. More interestingly, when moving down the chalcogen atoms X in In_2XO monolayers from S to Te, the band gap not only decreases, as when comparing In_2SO with In_2SeO, but even the In_2TeO monolayer is metal at equilibrium, as shown in Fig. 2(c). However, Perdew and Levy have demonstrated that the PBE calculations underestimate the band gap of insulators and semiconductors [46], and calculations using the hybrid functional [47] or GW approximation [48] can give more

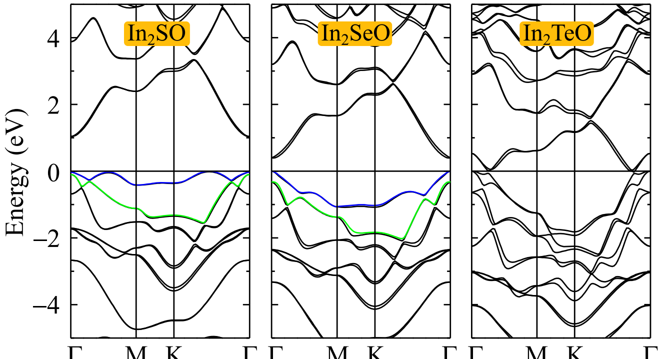

FIG. 3. Calculated band structures In_2XO using the PBE + SOC method.

accurate results. The calculated band structures of the In_2XO monolayer using the hybrid functional HSE06 are also presented in Fig. 2. We can see that the profiles of band structures at the HSE06 and PBE levels are the same. Additionally, although the band gap calculated using the HSE06 functional, as expected, is larger than that obtained by the PBE method for the In_2SO and In_2SeO monolayers, the In_2TeO monolayer still preserves its metallic characteristics. The band gaps of the In_2SO and In_2SeO monolayers at HSE06 level E_g^{HSE06} are 1.806 and 1.106 eV, respectively. Compared with Ga_2XO monolayers [35], the band gap of the In_2SO monolayer is smaller than that of Ga_2SO (2.08 eV), while the band gap of In_2SeO is bigger than that of Ga_2SeO (1.00 eV) [35]. Focusing on the band structures of the In_2SO and In_2SeO monolayers, as presented in Figs. 2(a) and 2(b), we realize that, while the In_2SeO monolayer has a direct band gap with both the conduction band minimum (CBM) and valence band maximum (VBM) located at the Γ point [Fig. 2(b)], In_2SO possesses the characteristics of an indirect semiconductor with the CBM at the Γ point and the VBM lying on the KΓ path. This is different from Ga_2XO monolayers, where both Ga_2SO and Ga_2SeO monolayers are direct semiconductors [35]. To estimate the contribution of orbitals to the formation of electronic bands, we calculated the density of states, as shown in Fig. 2. We can see that X-p and O-p orbitals have a remarkable contribution to the valence band. Additionally, the contribution of the X-s, In-d, and O-s orbitals to the conduction and valence bands is nearly equal.

It is noted that the SOC plays an important role in modification of the electronic properties of compounds, especially compounds based on heavy elements. The calculated band structures of the Janus In_2XO by the PBE + SOC is presented in Fig. 3. Our obtained results demonstrate that, while In_2TeO preserves its metallic characteristics, the SOC slightly reduces the band gap of both In_2SO and In_2SeO monolayers. When the SOC is included, the calculated band gap $E_g^{\text{PBE+SOC}}$ by the PBE + SOC method of In_2SO and In_2SeO is 1.042 and 0.401 eV, respectively (see also Table II for comparison with and without the SOC case). A weak influence of the SOC on the band structure of Ga_2SeTe has also been recently reported by Huang *et al.* [30]. Also, due to the SOC, a small spin-orbit splitting energy Δ is observed at the Γ point in the valence band. The value of the Δ depends strongly on the size of the

TABLE II. Calculated band gap E_g (eV) using the PBE, PBE+SOC, and HSE06 approaches and work functions of two different surfaces Φ_X (eV) and Φ_O (eV) of the Janus In_2XO monolayers (X = S, Se, Te).

	E_g^{PBE}	$E_g^{PBE+SOC}$	E_g^{HSE06}	Φ_X	Φ_O
In_2SO	1.084	1.042	1.806	6.48	5.80
In_2SeO	0.580	0.401	1.106	5.68	5.28
In_2TeO	Metal	Metal	Metal	4.16	4.16

elements. There is a significant difference in Δ between In_2SO and In_2SeO due to the difference in the atomic mass between S and Se. It is found that the spin-orbit splitting energy for In_2SO and In_2SeO is 0.078 and 0.325 eV, respectively.

It is well known that the influence of the dipole correction on the electrostatic potential distribution perpendicular to Janus structures is important [49]. Due to their asymmetric geometric structure, Janus monolayers have a built-in electric field [50]. Therefore, the dipole correction should be investigated for Janus structures. In Fig. 4, we show our calculations for the electrostatic potential with dipole correction of the Janus In_2XO monolayers, from which we can determine the work function of the monolayers. It is well known that the work function Φ refers to the ability of an electron to escape from the surface of the material. The work function is the minimum energy for an electron to move from the Fermi and vacuum levels. Once the dipole correction is included, there is a vacuum level difference between the two sides of the Janus In_2XO monolayers. Consequently, the work functions for two different surfaces Φ_X and Φ_O are different. Our obtained results reveal that the difference in work functions between two surfaces in In_2SO is largest at 0.68 eV with $\Phi_S = 6.48$ eV and $\Phi_O = 5.80$ eV. In the case of the In_2TeO monolayer, the difference in work functions is almost ignored with $\Phi_{Te} \approx \Phi_O = 4.16$ eV. The detailed calculation results for the work functions are also listed in Table II.

As mentioned above, the electronic properties of 2D nanomaterials are very sensitive to structural perfection, and strain engineering can significantly alter their electronic properties. In this part, we also calculate the influence of biaxial strain ε_b on band structures of the Janus structures, as shown in Fig. 5. Our calculations demonstrate that the indirect-direct band gap transition was observed in the In_2SO monolayer in

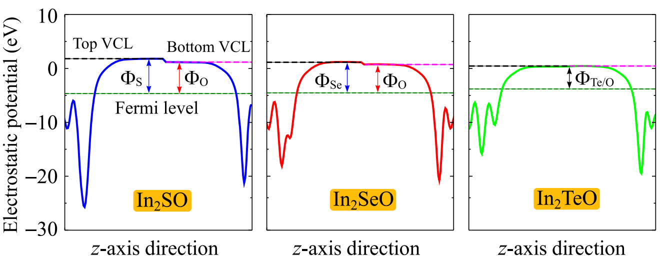

FIG. 4. Electrostatic potential of In_2XO monolayers. The work functions of two different surfaces Φ_X and Φ_O are measured via the vacuum and Fermi levels. The dashed black and purple lines refer to the top and bottom vacuum levels (VCL), respectively. The dashed dark green line refers to the Fermi level.

the presence of compression strain, as illustrated in Fig. 5(a). Additionally, the In_2SeO monolayer becomes an indirect gap semiconductor at large tensile biaxial strain $\varepsilon_b \leqslant 7\%$ with the moving of the VBM from the Γ point to the point on the ΓK path. As shown in Fig. 5(b), we can see the formation of the valence band inversion at $\varepsilon_b = 7\%$. However, the band inversion depth in the valence band of the In_2SeO monolayer at $\varepsilon_b = 7\%$ is very small, about 13 meV. The valence band inversion in GaSe has been also confirmed by angle-resolved photoemission spectroscopy [51]. When strain is applied, the atomic structure, including the bond lengths, of materials is changed. The change in bond length between atoms leads to the hopping energy changing [52]. This is one of the causes that leads to the change in band gap of materials. In fact, biaxial strain drastically changes the band gap of the In_2SO and In_2SeO monolayers, as shown in Figs. 5(a) and 5(b). More interestingly, the semiconductor-metal phase transition occurs at $\varepsilon_b = -7\%$. Under the compressive strain, the band gap of the In_2SeO monolayer drastically decreases and reaches zero at $\varepsilon_b = -7\%$. Figure 5(c) reveals that the metallic characteristics of the In_2TeO monolayer are still preserved in the strain range from −10% to 10%. In Fig. 6(a), we show our obtained calculations for biaxial strain dependence of the band gap of Janus In_2XO monolayers. We can see that the graph describing the dependence of band gaps of In_2SO and In_2SeO on the biaxial strain ε_b is quite similar in shape. When $\varepsilon_b \geqslant 5\%$, the band gaps of In_2SO and In_2SeO are almost the same. Compressive strain slightly increases the gap of In_2SO and then rapidly decreases almost linearly.

We also examined the influence of the electric field E on the band structures of the Janus monolayers, as shown in Fig. 7. A wide range of E from 0 to ±5 V/nm was applied to Janus structures. Previously, a strong electric field up to 3 V/nm has been experimentally applied to graphene [53]. Calculated results reveal that there is not much change in the band structures of the In_2SeO and In_2TeO monolayers when a perpendicular electric field with intensity ranging from −5 to 5 V/nm is applied. However, in the presence of the positive electric field, the VBM of In_2SO tends to shift from the KΓ path to the Γ point, as depicted in Fig. 7(a). As a consequence, the indirect-direct gap transition has been found in In_2SO at $E = +3$ V/nm. The band gaps of In_2XO are not significantly changed in the presence of the electric field. The dependence of their band gaps on the electric field is also presented in Fig. 6(b). The weak dependence of the band gap on the electric field has also been reported for other Janus group III monochalcogenide, such as the Ga_2SeTe monolayer [54].

V. TRANSPORT PROPERTIES

The carrier mobility in materials is one of the important properties that determines their applicability to electronic devices. The carrier mobility μ_{2D} of the studied Janus monolayers was estimated using deformation potential approximation, which can be written as [55–57]

$$\mu_{2D} = \frac{e\hbar^3 C_{2D}}{k_B T m^* \overline{m} E_d^2}, \quad (2)$$

FIG. 5. Band structures of (a) In_2SO, (b) In_2SeO, and (c) In_2TeO monolayers at different levels of biaxial strain ε_b.

where $\hbar$ is the Planck constant, e is the charge of an electron, T is the room temperature, k_B is the Boltzmann constant, C_{2D} is the elastic modulus, E_d is the deformation potential constant, and m^* and $\overline{m} = \sqrt{m_x^* m_y^*}$ are, respectively, the carrier effective masses and average effective mass.

The elastic modulus C_{2D} was predicted using the formula $C_{2D} = [\partial^2 E(k)/\partial \varepsilon^2]/S_0$, where $E(k)$ is the energy of an electron at a wave vector k in the VBM and CBM. The electron and hole effective masses in the transport direction m^* can be defined as

$$\frac{1}{m^*} = \frac{1}{\hbar}\frac{\partial^2 E(k)}{\partial k^2}. \tag{3}$$

The deformation potential constant E_d can be written as

$$E_d = \frac{\partial E_{\text{edge}}}{\partial \varepsilon}, \tag{4}$$

where E_{edge} signifies the energy change of CBM for electrons and VBM for holes as a function of uniaxial strain ε along x and y axes.

Due to the metallic characteristics of the In_2TeO monolayer, hereafter, we focus only on the In_2SO and In_2SeO monolayers. We first calculate the elastic modulus of the Janus structures. In Fig. 8, we show our calculations for the energy shifting and band edge positions of the In_2SO and In_2SeO monolayers. As shown in Fig. 8(b), we find that the band edge positions of the In_2SO and In_2SeO monolayers are independent of the direction of uniaxial strain. However, the energy shifting in the Janus structures, especially in the In_2SeO monolayer, depends strongly on the direction of uniaxial strain, i.e., the x and y directions. As a result, there is a large difference in the elastic modulus between the x and y directions in the Janus In_2SeO monolayer. The C_{2D}^x and C_{2D}^y for

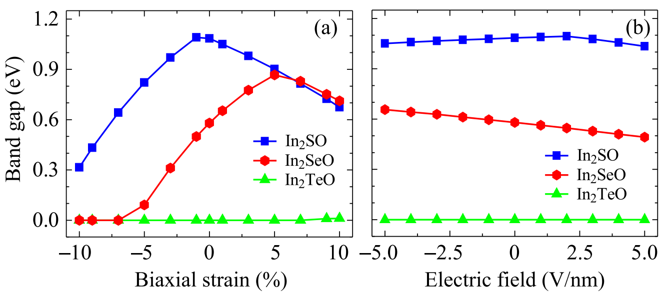

FIG. 6. Calculated band gap of the Janus In_2XO monolayers as a function of (a) biaxial strain and (b) electric field using the PBE functional.

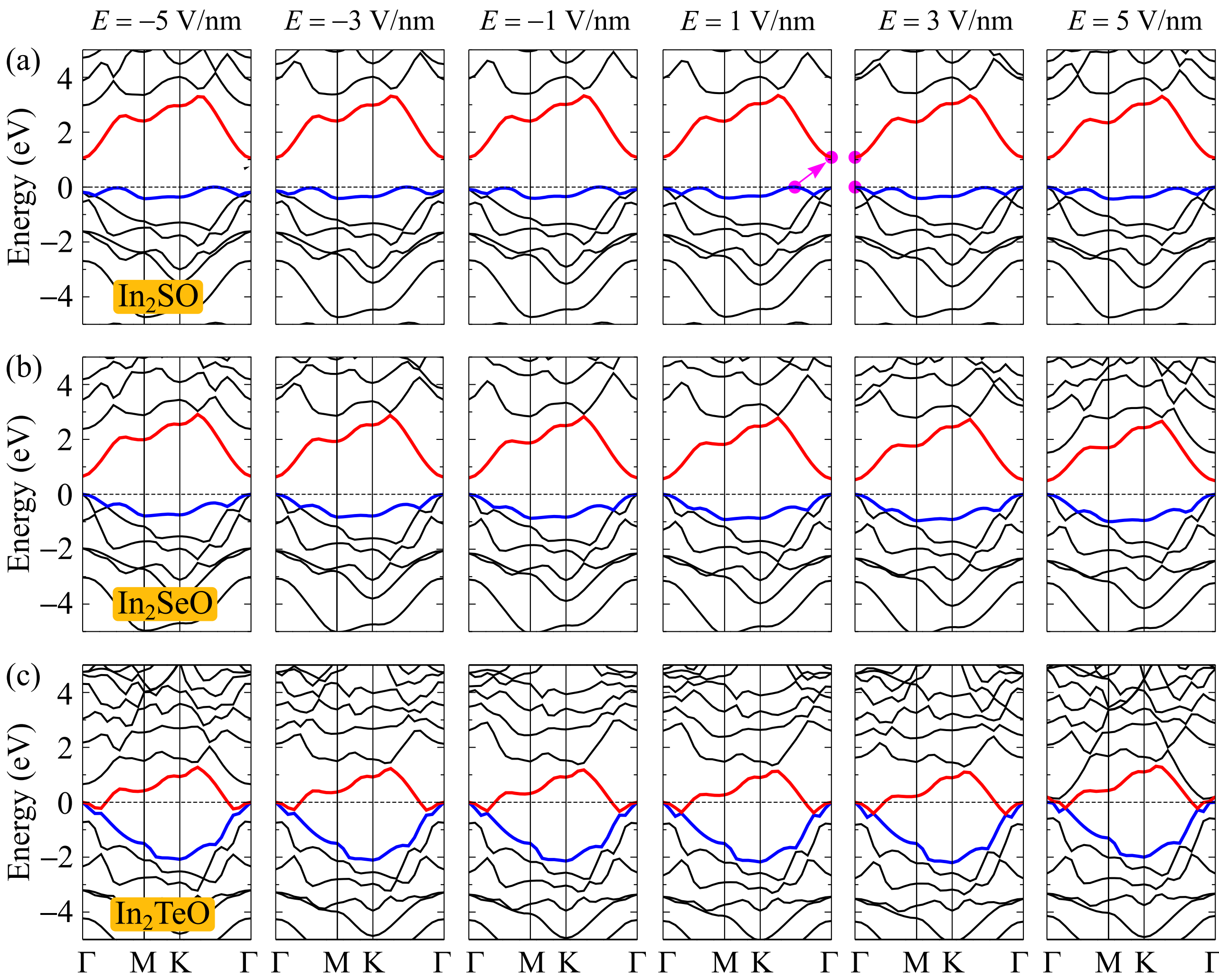

FIG. 7. Band structures of (a) In_2SO, (b) In_2SeO, and (c) In_2TeO monolayers at different values of electric field E.

the In_2SO monolayer are 76.93 and 91.21 N/m, respectively. The Janus In_2SeO monolayer exhibits an anisotropic in-plane stiffness which could be attributed to strain sensitivity along the x direction. The possible reason for such anisotropic behavior may be related to the minor distortion that happened during the geometry optimization at the In-Se and In-O sites in In_2SeO. The large difference in bond lengths between In-O and In-Se bonds in In_2SeO, as listed in Table I ($d_{\text{In-O}} = 2.245$ and 2.601 Å) leads to reduce in-plane symmetry of the hexagonal structure. This contributes to the anisotropic behavior of In_2SeO. The difference in bond length between the $d_{\text{In-O}}$ and $d_{\text{In-Se}}$ in In_2SeO is 0.356 Å, much larger than that between $d_{\text{In-O}}$ and $d_{\text{In-S}}$ in In_2SO (0.285 Å). The typical parameters for the transport properties of the Janus In_2SO and In_2SeO monolayers are listed in Table III. Our obtained results demonstrate that In_2SO has very high carrier mobility with anisotropic behavior where electrons and holes move along the different transport directions. In In_2SO, the electron mobility along the x axis μ_x is 3.428×10^3 (cm^2/Vs), about 1.23 times higher than that in the y axis ($\mu_y = 2.796 \times 10^3$ cm^2/Vs). The electron mobility of In_2SO is higher than that reported for both InSe (943.3 cm^2/Vs) and InSSe (884.8 cm^2/Vs) or InSeTe (1190.6 cm^2/Vs) monolayers [31]. Recently, the electron mobility in a few layers of InSe has been reported to be about 10^3 cm^2/Vs at room temperature [58]. In contrast, In_2SeO has a low carrier mobility with $\mu_x = 253$ cm^2/Vs and $\mu_y = 374$ cm^2/Vs. The carrier mobility of In_2SO is higher than that of In_2SeO because the effective mass m^* of In_2SO is smaller. As shown in Table III, we can see that the electron effective mass of In_2SO is $0.92m_0$ (m_0 is the free electron mass), which is smaller than that of the In_2SO monolayer ($1.20m_0$). With high carrier mobility and anisotropic behavior of carrier mobility, In_2XO has an advantage in applications for electronic devices.

VI. OPTICAL PROPERTIES

The optical characteristics can be derived from the dielectric constant defined as $\varepsilon(\omega) = \varepsilon_1(\omega) + i\varepsilon_2(\omega)$. The imaginary part $\varepsilon_2(\omega)$ is usually calculated first as follows [59,60]:

$$\varepsilon_2(\omega) = \frac{4\pi^2 e^2}{V m^2 \varpi^2} \sum_{nn'\sigma} \langle kn\sigma | p_i | kn'\sigma \rangle \langle kn'\sigma | p_j | kn\sigma \rangle \times f_{kn}(1 - f_{kn'})\delta(E_{kn'} - E_{kn} - \hbar\omega), \quad (5)$$

where e/m is the charge/mass of an electron, V is the unit-cell volume, $|knp\rangle$ is the wave function of the crystal with

TABLE III. The calculated effective mass m^*, deformation potential constant E_d, elastic modulus C_{2D}, and electron/hole mobility μ along x and y directions of In_2SO and In_2SeO Janus monolayers using PBE functional. Here, m_0 is the free electron mass.

Carrier type	Monolayer	m_x^* (m_0)	m_y^* (m_0)	E_d^x (eV)	E_d^y (eV)	C_{2D}^x (N/m)	C_{2D}^y (N/m)	μ_x (cm^2/Vs)	μ_y (cm^2/Vs)
Electron	In_2SO	0.92	0.97	0.76	0.82	80.68	80.75	3428	2796
	In_2SeO	1.20	1.30	2.08	1.79	76.93	91.21	253	374
Hole	In_2SO	1.94	1.39	0.76	0.82	80.68	80.75	935	1122
	In_2SeO	1.26	1.77	2.08	1.86	76.93	91.21	202	213

the momentum operator p, and f_{kn} is the Fermi distribution function. Using the Kramers-Kronig transformation, the real part $\varepsilon_1(\omega)$ can be derived from $\varepsilon_1(\omega)$ [61].

The absorption coefficient $A(\omega)$ can be derived from the parts of the dielectric function as follows [62]:

$$A(\omega) = \frac{\sqrt{2}\omega}{c}[\sqrt{\varepsilon_1(\omega)^2 + \varepsilon_2(\omega)^2} - \varepsilon_1(\omega)]^{1/2}. \quad (6)$$

Owing to its metallic characteristics, the In_2TeO monolayer can strongly absorb light in the low energy region. We only focus on semiconducting Janus In_2SO and In_2SeO monolayers with the incoming photon energy range to be studied from 0 to 10 eV. In Fig. 9, we show our obtained results for the imaginary part $\varepsilon_2(\omega)$ of the dielectric function and absorption coefficient of the In_2SO and In_2SeO monolayers by using both the PBE and HSE06 functionals. For the In_2SO monolayer, the optical absorption is activated at 1.10 and 1.78 eV by the PBE and HSE06 calculations, respectively. In the case of the In_2SeO monolayer, the activation threshold for optical absorption lies entirely in the infrared region, at 0.53 eV by the PBE approach and 1.18 eV by the HSE06 approach. These activation thresholds for optical absorption perfectly coincide with the direct gap values of the In_2SO and In_2SeO monolayers. At the HSE06 level, the first peak in the absorption spectrum of both In_2SO and In_2SeO monolayers is in the near-ultraviolet region (about 4 eV), and the absorption intensity of the monolayers is strongly increased in this region. This suggests that the Janus In_2SO and In_2SeO monolayers can be applied in optoelectronic devices.

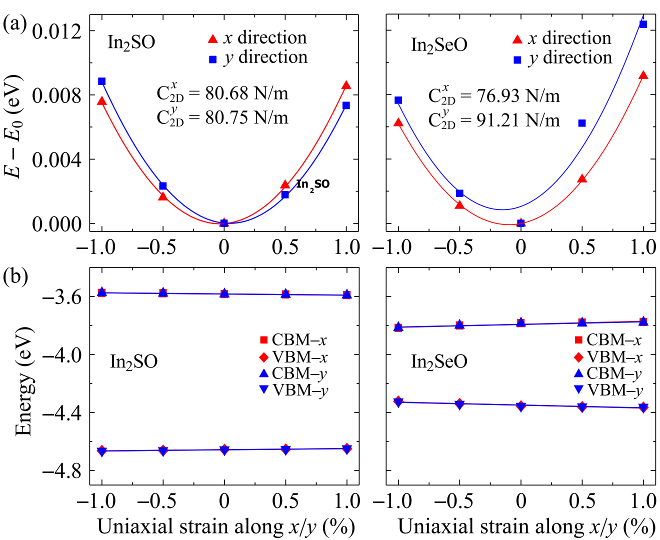

FIG. 8. (a) The energy shifting and (b) the band edge positions of In_2SO and In_2SeO monolayers with respect to uniaxial strain along x and y directions using the PBE approach.

VII. THERMOELECTRIC PROPERTIES

Since 1993, Hicks and Dresselhaus have predicted that low dimensional structures can be used as thermal materials [63], and the figure of merit is the key factor to describe the thermoelectric conversion efficiency of materials. The figure of merit ZT is calculated by the formula [64]

$$ZT = S^2\sigma T\frac{1}{\kappa_e + \kappa_l}, \quad (7)$$

where S and σ are, respectively the Seebeck coefficient and the electrical conductivity, T is the temperature, and κ_l and κ_e refer, respectively, to the lattice and electronic parts of the thermal conductivity.

The relaxation time τ is an important parameter of the thermoelectric properties. The τ depends strongly on the scattering processes, such as impurities and phonons. The relaxation time can be calculated via the mobility μ_{2D} suggested by the expression [65,66] $\tau = m^*\mu_{2D}/e$, where m^* is the effective mass, and μ_{2D} is given by Eq. (2). Previously, Kaasbjerg *et al.* have demonstrated that the carrier mobility of

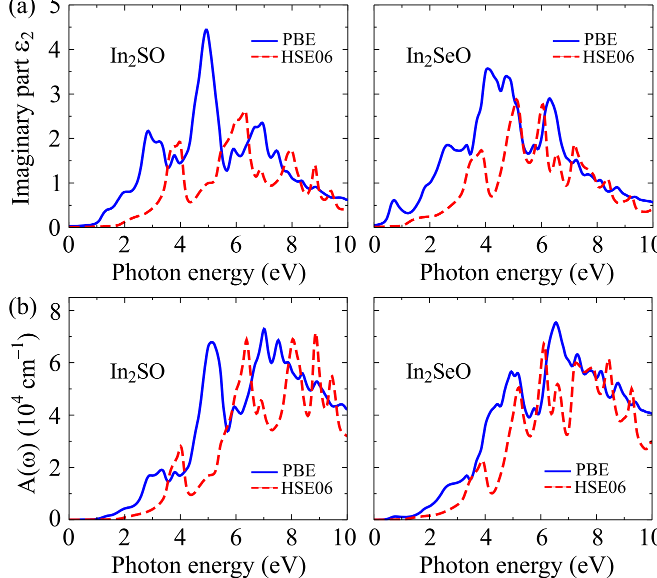

FIG. 9. Imaginary parts of the dielectric function and absorption coefficient of (a) In_2SO and (b) In_2SeO monolayers.

TABLE IV. Interlayer distance h (Å) and band gap at the PBE E_g^{PBE} (eV) and HSE06 E_g^{HSE06} (eV) levels, and binding energy E_b (eV) of the In_2SO and In_2SeO bilayers with different stacking configurations.

	AA				AA′				AB				AB′			
Bilayer	h	E_g^{PBE}	E_g^{HSE}	E_b	h	E_g^{PBE}	E_g^{HSE}	E_b	h	E_g^{PBE}	E_g^{HSE}	E_b	h	E_g^{PBE}	E_g^{HSE}	E_b
In_2SO	3.864	0.791	1.318	−0.168	4.114	1.064	1.787	−0.123	3.333	0.594	1.024	−0.230	3.362	0.969	1.711	−0.192
In_2SeO	3.720	0.402	0.73	−0.218	3.952	0.509	1.061	−0.166	3.215	0.078	0.276	−0.353	3.357	0.449	1.001	−0.267

2D materials is not sensitive to the carrier concentration [67]. Therefore, we suggest that the relaxation time is independent on the doping level N.

Our calculations reveal that the relaxation time of In_2SO is close to that of In_2SeO. At room temperature, the relaxation time of In_2SO and In_2SeO is 7.45×10^{-15} and 7.14×10^{-15} s, respectively. Previously, the relaxation time at 300 K for MoS_2 was reported as 5.17×10^{-14} s [66]. The temperature-dependent relaxation time of the In_2SO and In_2SeO monolayers is presented in Fig. 10. We can see that relaxation time rapidly decreases with temperature increasing. At 1000 K, the relaxation time of In_2SO and In_2SeO is about 1.2×10^{-15} s.

By solving the Boltzmann transport equation with the constant relaxation time and rigid band approximation, we investigate the electronic transport coefficients of Janus structures, including the Seebeck coefficient S, electrical conductivity σ, and power factor $S^2\sigma$ via the PBE method. These transport coefficients are estimated as a function of the doping level N. In the low-dimensional nanomaterials, the doping level N stands for the number of electrons/holes per unit cell. The positive (negative) value of N refers to the $p(n)$-type doping. The electronic transport coefficients of In_2SO and In_2SeO at room temperature (300 K) are presented in Fig. 11. It is found that there is no significant difference in transport coefficients, including the Seebeck coefficient S, σ, and $S^2\sigma$, in the n-type doping case. In the p-type doping case, the difference in σ between In_2SO and In_2SeO is obvious. Compared with the In_2SO monolayer, the electrical conductivity σ of In_2SeO increases rapidly with doping level N in the case of p-type doping. In the doping level range from −0.04 to 0.04, as shown in Fig. 11(c), there is a big difference in the changing trend of the power factor $S^2\sigma$ in the case of $N > 0$. The power factor of In_2SeO increases slightly and reaches the maximum value at $N = 0.012$ and then begins to decrease slowly. Meanwhile, the power factor in In_2SO increases rapidly when N varies from 0 to 0.04.

The important parameter of thermal materials is the dimensionless figure of merit ZT, as presented in Eq. (7). The figure of merit depends strongly on the total thermal conductivity κ_{tot} ($\kappa_{\mathrm{tot}} = \kappa_e + \kappa_l$). The calculated parts of the thermal conductivity of In_2SO and In_2SeO at room temperature are shown in Fig. 12. We can see that, as shown in Fig. 12(a),

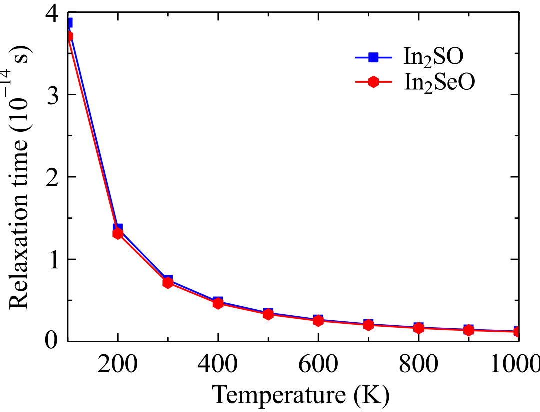

FIG. 10. Relaxation time of the In_2SO and In_2SeO monolayers.

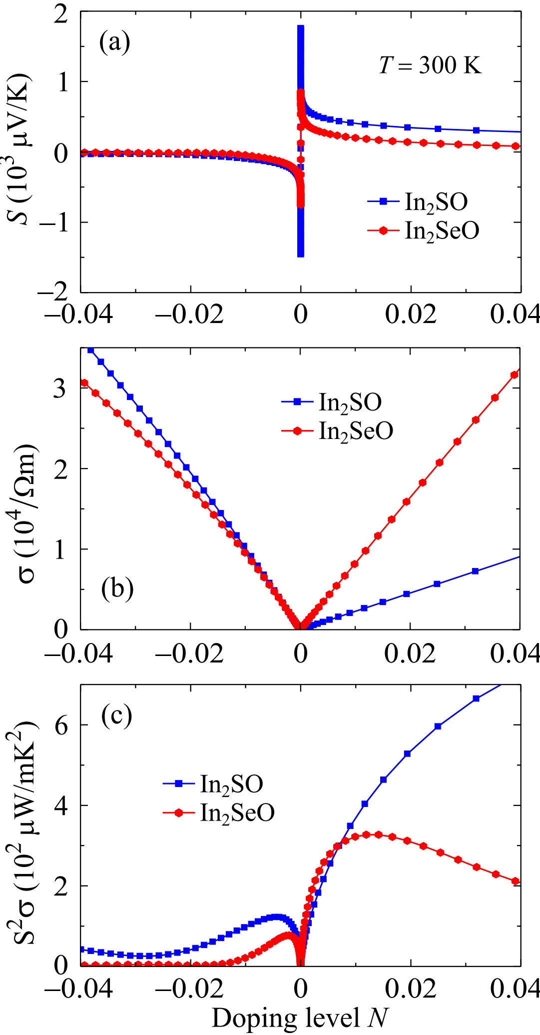

FIG. 11. (a) Seebeck coefficient S, (b) electrical conductivity σ, and (c) power factor $S^2\sigma$ as a function of the doping level N at 300 K of the In_2SO and In_2SeO monolayers.

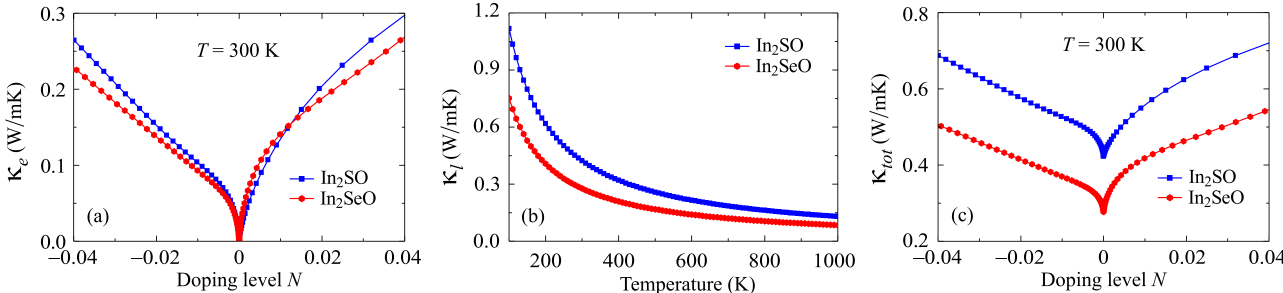

FIG. 12. (a) Doping level N dependent electronic thermal conductivity κ_e at room temperature, (b) temperature dependent lattice thermal conductivity κ_l, and (c) doping level N dependent total thermal conductivity κ_{tot} at room temperature of In_2SO and In_2SeO monolayers.

the electronic thermal conductivity κ_e increases rapidly with the doping level N, for both cases of n and p doping. Also, there is no big difference in κ_e between In_2SO and In_2SeO in the small range of the doping level. The most important parameter for the thermoelectric figure of merit is the lattice thermal conductivity κ_l, which is assumed to be doping level independent [66,68]. Our obtained results demonstrate that both In_2SO and In_2SeO exhibit an ultralow lattice thermal conductivity κ_l. At 300 K, the lattice thermal conductivity of In_2SO and In_2SeO is 0.423 and 0.277 W/mK, respectively. These values are close to κ_l of TlInTe2 (0.370 W/mK) [69], but they are much lower than the lattice thermal conductivity of the HfSSe monolayer (1.78 W/mK) [70]. As expected, the κ_l of the Janus structures becomes lower at higher temperatures. The κ_l of In_2SO and In_2SeO at 900 K is only 0.144 and 0.094 W/mK, respectively. The temperature dependence of the κ_l is presented in Fig. 12(b). In a semiconductor, the phonons have a great contribution to the thermal conductivity. The total thermal conductivity κ_{tot} as a function of the doping level is shown in Fig. 12(c). We can see that due to the large contribution from the lattice thermal conductivity κ_l, the κ_{tot} of In_2SO is higher than that of In_2SeO.

Due to the low thermal conductivity, the figure of merit ZT of the Janus structures In_2SO and In_2SeO is expected to be high, especially in high temperatures. Our calculated results demonstrate that the ZT for the p-type doping of the In_2SO and In_2SeO monolayers is higher than that for the n-type doping. At room temperature, while the peak of ZT for the n-type doping of In_2SO (In_2SeO) is only 0.075 (0.071), the maximum ZT for the p-type doping of In_2SeO is up to 0.231 at $N = 0.01$. The dependence of the figure of merit on the doping level at different values of temperature is depicted in Fig. 13. It is found that the ZT of the Janus structures increases strongly with the temperature increasing, especially the p-type ZT of In_2SeO increases rapidly with temperature. At 900 K, the p-type ZT of In_2SeO reaches 0.8 at N around 0.35, as shown in Fig. 13(b). In the case of In_2SeO, the ZT value only increases slightly with temperature, especially in the case of p-type doping. In the doping level range from -0.04 to 0.04, the ZT value of In_2SO does not exceed 0.5, as depicted in Fig. 13(a). Although the figure of merit does not exceed one, with low thermal conductivity, Janus structures, especially the In_2SeO monolayer, have great prospects of being used as thermoelectric materials.

VIII. BILAYER JANUS In_2XO STRUCTURES

In this section, we briefly investigate the structural and electronic properties of the bilayers of Janus In_2XO. The In_2TeO bilayer was excluded in this examination due to the metallic characteristics of its monolayer structure. There are four possible staking configurations of the bilayers of In_2XO structures, as shown in Fig. 14. As shown in Fig. 14, the AA configuration corresponding to the case of two Janus layers is precisely placed on top of each other, while the AB configuration is designed such that the atom In of the top layer is located directly above the X atom of the bottom layer. The AA′ and

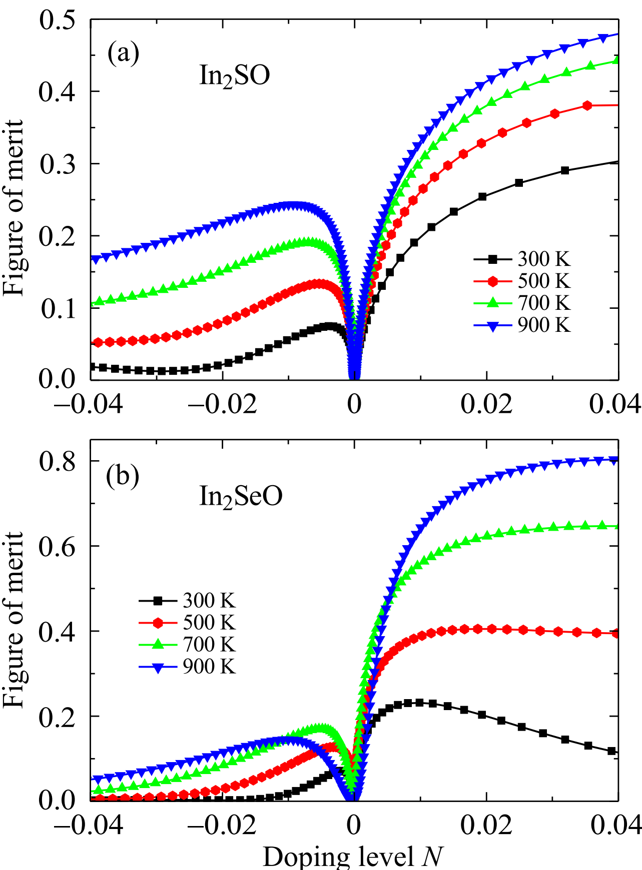

FIG. 13. Figure of merit of (a) In_2SO and (b) In_2SeO monolayers as a function of doping level N at different values of temperature.

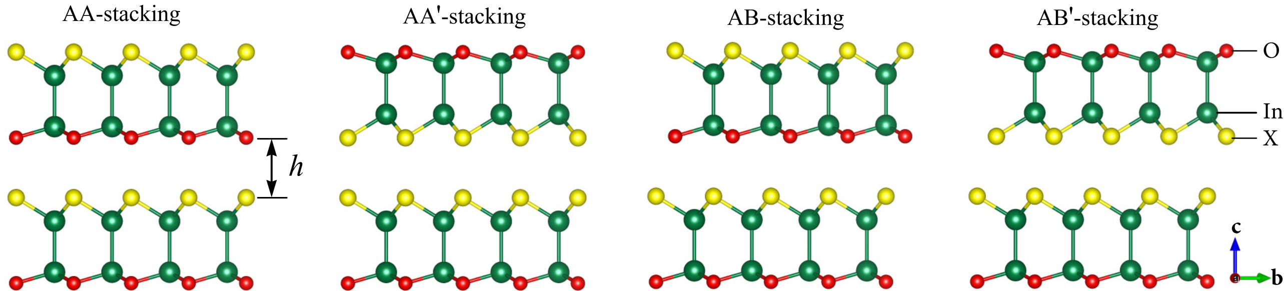

FIG. 14. Different stacking configurations of bilayer In_2XO. Green, yellow, and red balls refer to the In, X, and O atoms, respectively.

AB′ stacking configurations are, respectively, similar to the AA and AB configurations, but the top layers are inverted. The distance between layers h depends not only on the size of the X atom but also on the stacking configuration. For each stacking configuration, the interlayer distance h of the In_2SO bilayer is larger than that of In_2SeO. The largest interlayer distance corresponds to the AA′ configuration for both In_2SO and In_2SeO bilayers, as listed in Table IV. Meanwhile, the AB configuration has the smallest interlayer distance corresponding to 3.333 and 3.215 Å for In_2SO and In_2SeO bilayers, respectively.

To test the stability of the Janus bilayers, we calculate the phonon spectra of all four stacking configurations of the In_2SO and In_2SeO bilayers, which are presented in Fig. 15. Our obtained results demonstrate that both In_2SO and In_2SeO bilayers with all four stacking configurations AA, AA′, AB, and AB′ are dynamically stable. Also, we calculate the binding energy E_b of the Janus bilayers, which is written as

$$E_b = E_{\text{bilayer}} - (E_{\text{top}} + E_{\text{bottom}}), \tag{8}$$

where E_{bilayer} is the total energy of the bilayer, while E_{top} and E_{bottom} are the total energies of the top and bottom layers, respectively. Our obtained results, as presented in Table IV, demonstrate that the binding energy E_b is between −0.123 eV (In_2SO with AA' stacking) and −0.353 eV (AB configuration of In_2SeO). This indicates that there are van der Waals interactions between monolayers in the bilayers. By comparing the total energies between configurations, we can see that AB stacking is the ground state configuration for both In_2SO and In_2SeO bilayers.

In Fig. 16, we show our calculated results for the band structures of the In_2XO bilayers by using the HSE06 functional. Similar to the monolayer, the In_2TeO bilayer is

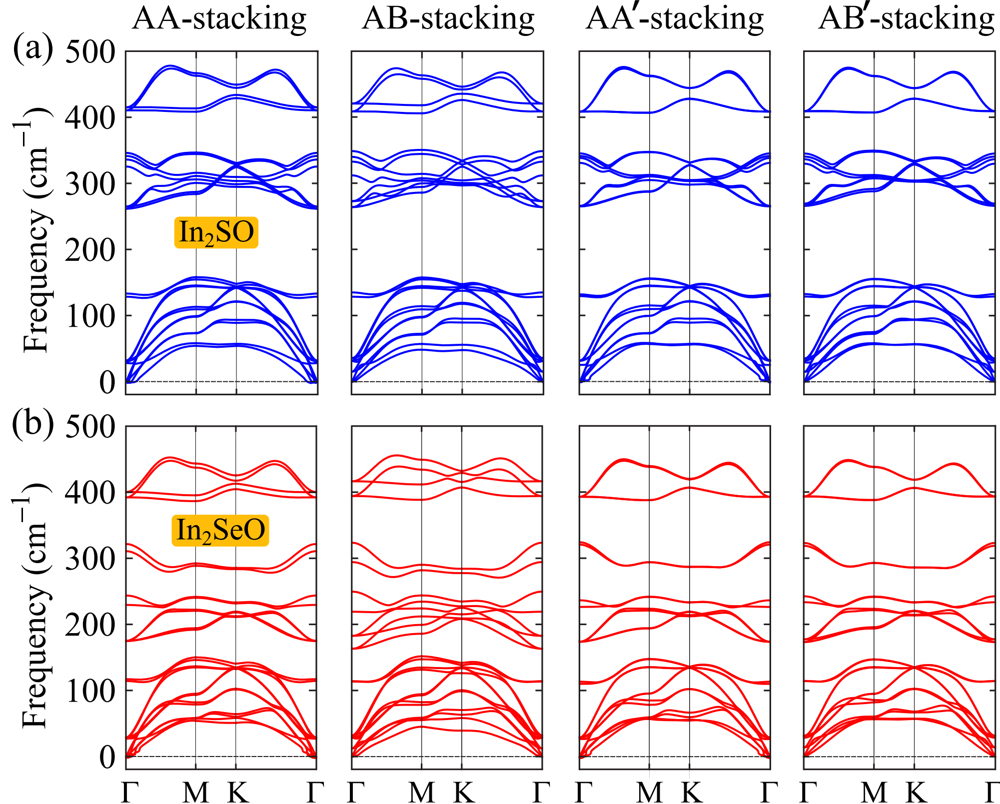

FIG. 15. Phonon spectra of bilayers (a) In_2SO and (b) In_2SeO with different stacking configurations.

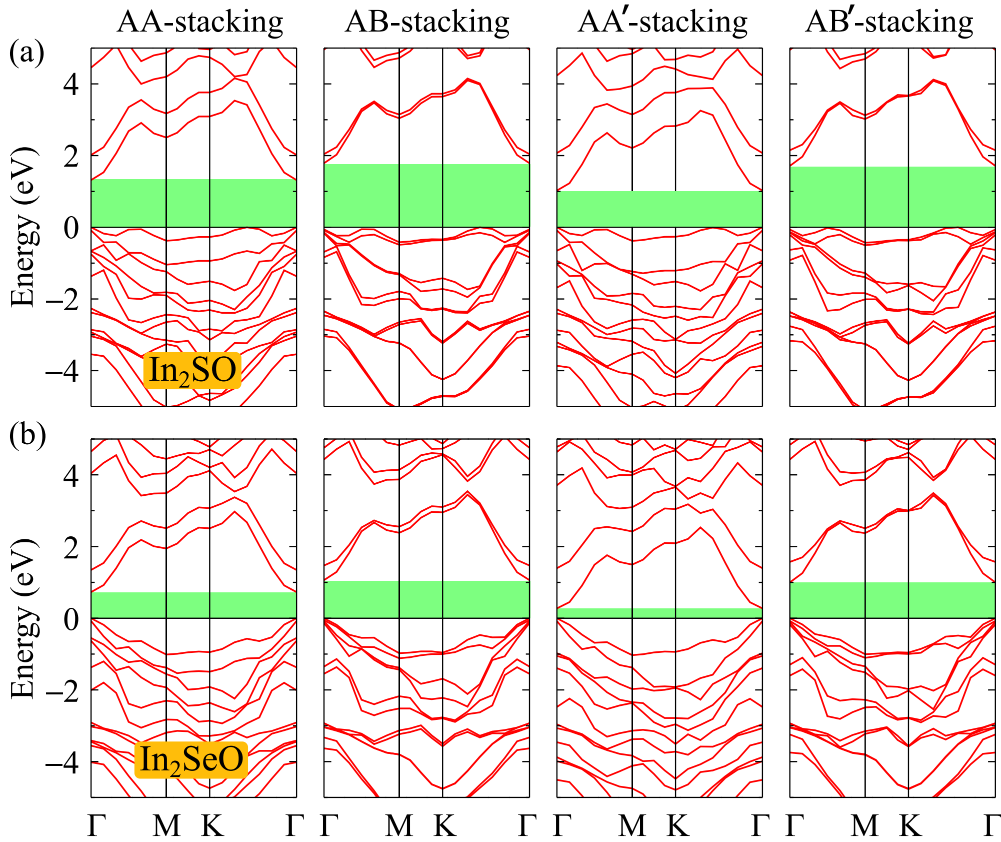

FIG. 16. Band structures of four stacking configurations AA, AA′, AB, and AB′ of bilayers (a) In_2SO and (b) In_2SeO.

still a metal for all stacking configurations. As depicted in Figs. 16(a) and 16(b), we can see that both In_2SO and In_2SeO bilayers preserve the semiconducting behavior. The highest band gap is observed for the AA′ configuration. The calculated band gaps of the In_2SO and In_2SeO bilayers with AA′ configuration are, respectively, 1.787 and 1.061 eV by the HSE06 approach, which is slightly lower than those of the monolayers. Meanwhile, the band gap for the AB stacking is the smallest, being 1.024 eV for the In_2SO bilayer and 0.276 eV for the In_2SeO bilayer. The band gaps of all stacking configurations are also presented in Table IV. Although their band gap decreases when forming a bilayer structure, however, the indirect semiconductor characteristics of In_2SO and the direct semiconductor of In_2SeO remain in the bilayer structures.

IX. CONCLUSIONS

In conclusion, we systematically investigated the basic physical properties of the Janus monolayers In_2XO (X = S, Se, Te) and bilayers In_2XO by using first-principles calculations based on DFT. Obtained results demonstrated that the In_2SO and In_2SeO monolayers, semiconductors with a moderate band gap, are dynamically stable. Their electronic properties are sensitive to the applied biaxial strain. Also, the value of the carrier mobility of In_2SO exceeds 3×10^3 cm^2/Vs and is higher than that of the In_2SeO monolayer. The activation threshold for optical absorption of the In_2SO and In_2SeO monolayers lies in the infrared region by the PBE approach, which is consistent with their direct gap values. The In_2SO and In_2SeO monolayers possess high values of the figure of merit, which is suitable for the thermal materials. The bilayers In_2SO and In_2SeO were constructed and investigated briefly. Obtained results indicated that the band gaps of the In_2SO and In_2SeO bilayers depend strongly on the stacking configuration. With the high optical absorption coefficient in the near-ultraviolet region and the indirect-direct band gap and semiconductor-metal phase transitions found in the presence of strain, Janus monolayers In_2XO are expected to be applied to optoelectronic devices.

ACKNOWLEDGMENTS

This research is funded by the Vietnam National Foundation for Science and Technology Development (NAFOSTED) under Grant No. 103.01-2018.334.

[1] Q. Tang and Z. Zhou, Prog. Mater. Sci. **58**, 1244 (2013).
[2] A. I. Siahlo, N. A. Poklonski, A. V. Lebedev, I. V. Lebedeva, A. M. Popov, S. A. Vyrko, A. A. Knizhnik, and Y. E. Lozovik, Phys. Rev. Mater. **2**, 036001 (2018).
[3] N. A. Poklonski, S. A. Vyrko, A. I. Siahlo, O. N. Poklonskaya, S. V. Ratkevich, N. N. Hieu, and A. A. Kocherzhenko, Mater. Res. Express **6**, 042002 (2019).

[4] K. S. Novoselov, A. K. Geim, S. V. Morozov, D. Jiang, Y. Zhang, S. V. Dubonos, I. V. Grigorieva, and A. A. Firsov, Science **306**, 666 (2004).
[5] B. Lalmi, H. Oughaddou, H. Enriquez, A. Kara, S. Vizzini, B. Ealet, and B. Aufray, Appl. Phys. Lett. **97**, 223109 (2010).
[6] D. Kong, H. Wang, J. J. Cha, M. Pasta, K. J. Koski, J. Yao, and Y. Cui, Nano Lett. **13**, 1341 (2013).
[7] G. Deokar, D. Vignaud, R. Arenal, P. Louette, and J.-F. Colomer, Nanotechnology **27**, 075604 (2016).
[8] M. E. Dávila, L. Xian, S. Cahangirov, A. Rubio, and G. Le Lay, New J. Phys. **16**, 095002 (2014).
[9] F.-F. Zhu, W.-J. Chen, Y. Xu, C.-L. Gao, D.-D. Guan, C.-H. Liu, D. Qian, S.-C. Zhang, and J.-F. Jia, Nat. Mater. **14**, 1020 (2015).
[10] D. Muoi, N. N. Hieu, C. V. Nguyen, B. D. Hoi, H. V. Nguyen, N. D. Hien, N. A. Poklonski, S. S. Kubakaddi, and H. V. Phuc, Phys. Rev. B **101**, 205408 (2020).
[11] C. V. Nguyen, N. N. Hieu, N. A. Poklonski, V. V. Ilyasov, L. Dinh, T. C. Phong, L. V. Tung, and H. V. Phuc, Phys. Rev. B **96**, 125411 (2017).
[12] N. D. Hien, C. V. Nguyen, N. N. Hieu, S. S. Kubakaddi, C. A. Duque, M. E. Mora-Ramos, L. Dinh, T. N. Bich, and H. V. Phuc, Phys. Rev. B **101**, 045424 (2020).
[13] K. D. Pham, N. N. Hieu, H. V. Phuc, I. A. Fedorov, C. A. Duque, B. Amin, and C. V. Nguyen, Appl. Phys. Lett. **113**, 171605 (2018).
[14] D. D. Vaughn, R. J. Patel, M. A. Hickner, and R. E. Schaak, J. Am. Chem. Soc. **132**, 15170 (2010).
[15] P. Hu, L. Wang, M. Yoon, J. Zhang, W. Feng, X. Wang, Z. Wen, J. C. Idrobo, Y. Miyamoto, D. B. Geohegan, and K. Xiao, Nano Lett. **13**, 1649 (2013).
[16] P. Hu, Z. Wen, L. Wang, P. Tan, and K. Xiao, ACS Nano **6**, 5988 (2012).
[17] S. Acharya, M. Dutta, S. Sarkar, D. Basak, S. Chakraborty, and N. Pradhan, Chem. Mater. **24**, 1779 (2012).
[18] W. Feng, X. Zhou, W. Q. Tian, W. Zheng, and P. Hu, Phys. Chem. Chem. Phys. **17**, 3653 (2015).
[19] S. Demirci, N. Avazli, E. Durgun, and S. Cahangirov, Phys. Rev. B **95**, 115409 (2017).
[20] G. Shen, D. Chen, P.-C. Chen, and C. Zhou, ACS Nano **3**, 1115 (2009).
[21] H. L. Zhuang and R. G. Hennig, Chem. Mater. **25**, 3232 (2013).
[22] Y. Cui, L. Peng, L. Sun, Q. Qian, and Y. Huang, J. Mater. Chem. A **6**, 22768 (2018).
[23] A.-Y. Lu, H. Zhu, J. Xiao, C.-P. Chuu, Y. Han, M.-H. Chiu, C.-C. Cheng, C.-W. Yang, K.-H. Wei, Y. Yang, Y. Wang, D. Sokaras, D. Nordlund, P. Yang, D. A. Muller, M.-Y. Chou, X. Zhang, and L.-J. Li, Nat. Nanotechnol. **12**, 744 (2017).
[24] J. Zhang, S. Jia, I. Kholmanov, L. Dong, D. Er, W. Chen, H. Guo, Z. Jin, V. B. Shenoy, L. Shi, and J. Lou, ACS Nano **11**, 8192 (2017).
[25] Dimple, N. Jena, A. Rawat, R. Ahammed, M. K. Mohanta, and A. De Sarkar, J. Mater. Chem. A **6**, 24885 (2018).
[26] H. Li, Y. Qin, B. Ko, D. B. Trivedi, D. Hajra, M. Y. Sayyad, L. Liu, S.-H. Shim, H. Zhuang, and S. Tongay, Adv. Mater. **32**, 2002401 (2020).
[27] T. V. Vu, N. V. Hieu, H. V. Phuc, N. N. Hieu, H. Bui, M. Idrees, B. Amin, and C. V. Nguyen, Appl. Surf. Sci. **507**, 145036 (2020).
[28] H. T. T. Nguyen, V. V. Tuan, C. V. Nguyen, H. V. Phuc, H. D. Tong, S.-T. Nguyen, and N. N. Hieu, Phys. Chem. Chem. Phys. **22**, 11637 (2020).
[29] M. Yagmurcukardes, Y. Qin, S. Ozen, M. Sayyad, F. M. Peeters, S. Tongay, and H. Sahin, Appl. Phys. Rev. **7**, 011311 (2020).
[30] A. Huang, W. Shi, and Z. Wang, J. Phys. Chem. C **123**, 11388 (2019).
[31] W. Wan, S. Zhao, Y. Ge, and Y. Liu, J. Phys.: Conden. Matter **31**, 435501 (2019).
[32] Y. Guo, S. Zhou, Y. Bai, and J. Zhao, A, Appl. Phys. Lett. **110**, 163102 (2017).
[33] A. Kandemir and H. Sahin, Phys. Rev. B **97**, 155410 (2018).
[34] H. Yang, P. Zhao, Y. Ma, X. Lv, B. Huang, and Y. Dai, J. Phys. D: Appl. Phys. **52**, 455303 (2019).
[35] Y. Cui, L. Peng, L. Sun, M. Li, X. Zhang, and Y. Huang, J. Phys.: Condens. Matter **32**, 08LT01 (2020).
[36] M. Yagmurcukardes and F. M. Peeters, Phys. Rev. B **101**, 155205 (2020).
[37] M. Demirtas, B. Ozdemir, Y. Mogulkoc, and E. Durgun, Phys. Rev. B **101**, 075423 (2020).
[38] P. Giannozzi *et al.*, J. Phys.: Condens. Matter **21**, 395502 (2009).
[39] J. P. Perdew, K. Burke, and M. Ernzerhof, Phys. Rev. Lett. **77**, 3865 (1996).
[40] S. Grimme, J. Comput. Chem. **27**, 1787 (2006).
[41] A. H. MacDonald, W. E. Picket, and D. D. Koelling, J. Phys. C: Solid State Phys. **13**, 2675 (1980).
[42] T. Sohier, M. Calandra, and F. Mauri, Phys. Rev. B **96**, 075448 (2017).
[43] S. Nosé, J. Chem. Phys. **81**, 511 (1984).
[44] G. K. Madsen and D. J. Singh, Comput. Phys. Commun. **175**, 67 (2006).
[45] A. Togo, L. Chaput, and I. Tanaka, Phys. Rev. B **91**, 094306 (2015).
[46] J. P. Perdew and M. Levy, Phys. Rev. Lett. **51**, 1884 (1983).
[47] J. Heyd, G. E. Scuseria, and M. Ernzerhof, J. Chem. Phys. **118**, 8207 (2003).
[48] L. Hedin, Phys. Rev. **139**, A796 (1965).
[49] L. Bengtsson, Phys. Rev. B **59**, 12301 (1999).
[50] C.-F. Fu, J. Sun, Q. Luo, X. Li, W. Hu, and J. Yang, Nano Lett. **18**, 6312 (2018).
[51] Z. Ben Aziza, V. Zólyomi, H. Henck, D. Pierucci, M. G. Silly, J. Avila, S. J. Magorrian, J. Chaste, C. Chen, M. Yoon, K. Xiao, F. Sirotti, M. C. Asensio, E. Lhuillier, M. Eddrief, V. I. Fal'ko, and A. Ouerghi, Phys. Rev. B **98**, 115405 (2018).
[52] V. M. Pereira, A. H. Castro Neto, and N. M. R. Peres, Phys. Rev. B **80**, 045401 (2009).
[53] K. F. Mak, C. H. Lui, J. Shan, and T. F. Heinz, Phys. Rev. Lett. **102**, 256405 (2009).
[54] T. V. Vu, V. T. T. Vi, C. V. Nguyen, H. V. Phuc, and N. N. Hieu, J. Phys. D: Appl. Phys. **53**, 455302 (2020).
[55] J. Bardeen and W. Shockley, Phys. Rev. **80**, 72 (1950).
[56] S. Bruzzone and G. Fiori, Appl. Phys. Lett. **99**, 222108 (2011).
[57] R. Fang, X. Cui, M. A. Khan, C. Stampfl, S. P. Ringer, and R. Zheng, Adv. Electron. Mater. **5**, 1800797 (2019).
[58] D. A. Bandurin, A. V. Tyurnina, G. L. Yu, A. Mishchenko, V. Zólyomi, S. V. Morozov, R. K. Kumar, R. V. Gorbachev, Z. R. Kudrynskyi, S. Pezzini, Z. D. Kovalyuk, U. Zeitler, K. S. Novoselov, A. Patanè, L. Eaves, I. V. Grigorieva, V. I. Fal'ko, A. K. Geim, and Y. Cao, Nat. Nanotechnol. **12**, 223 (2017).

[59] A. Delin, P. Ravindran, O. Eriksson, and J. Wills, Int. J. Quantum Chem. **69**, 349 (1998).
[60] S. Z. Karazhanov, P. Ravindran, A. Kjekshus, H. Fjellvag, and B. G. Svensson, Phys. Rev. B **75**, 155104 (2007).
[61] H. Wang, G. Qin, J. Yang, Z. Qin, Y. Yao, Q. Wang, and M. Hu, J. Appl. Phys. **125**, 245104 (2019).
[62] P. Ravindran, A. Delin, B. Johansson, O. Eriksson, and J. M. Wills, Phys. Rev. B **59**, 1776 (1999).
[63] L. D. Hicks and M. S. Dresselhaus, Phys. Rev. B **47**, 16631 (1993).
[64] Y. Pei, X. Shi, A. LaLonde, H. Wang, L. Chen, and G. J. Snyder, Nature **473**, 66 (2011).
[65] D. Yu, Y. Zhang, and F. Liu, Phys. Rev. B **78**, 245204 (2008).
[66] Z. Jin, Q. Liao, H. Fang, Z. Liu, W. Liu, Z. Ding, T. Luo, and N. Yang, Sci. Rep. **5**, 18342 (2015).
[67] K. Kaasbjerg, K. S. Thygesen, and K. W. Jacobsen, Phys. Rev. B **85**, 115317 (2012).
[68] W. Huang, H. Da, and G. Liang, J. Appl. Phys. **113**, 104304 (2013).
[69] G. Ding, J. He, Z. Cheng, X. Wang, and S. Li, J. Mater. Chem. C **6**, 13269 (2018).
[70] D, M. K. Mohanta, A. Rawat, N. Jena, R. Ahammed, and A. De Sarkar, J. Phys.: Conden. Matter **32**, 315301 (2020).